Research Square

Preprints are preliminary reports that have not undergone peer review.
They should not be considered conclusive, used to inform clinical practice,
or referenced by the media as validated information.

Spatiotemporal Regulation and Functional Divergence of Bmp2 and Bmp7 in Periodontal Injury Response

Daniel Graf

daniel.graf@ubc.ca

University of British Columbia https://orcid.org/0000-0003-1163-8117

Yu Fu

University of British Columbia

Daniela Marta Roth

Cancer Early Detection Advanced Research Center (CEDAR)

Maria Alexiou

The University of British Columbia

Article

Keywords: Bone morphogenetic protein (Bmp), Bmp2, Bmp7, periodontal ligament stem cells (PDLSCs), Gli1+ stem cells, alveolar bone regeneration, ligature-induced periodontitis

Posted Date: June 10th, 2026

DOI: https://doi.org/10.21203/rs.3.rs-9657888/v1

License: This work is licensed under a Creative Commons Attribution 4.0 International License.
Read Full License

Additional Declarations: There is no conflict of interest

Abstract

Teeth are anchored to the alveolar bone by the periodontal ligament (PDL), which harbors stem cells that support tissue turnover. Severe periodontitis destroys the periodontium and is a major cause of adult tooth loss. Bone morphogenetic proteins (Bmps) facilitate osteoblast differentiation and contribute to periodontium homeostasis; however, the *in vivo* contribution of individual Bmp family members in coordinating tissue regeneration following a periodontal injury remains unclear. Using a ligature-induced periodontal injury mouse model, we first tracked the spatiotemporal expression of Bmp2 and Bmp7 during periodontium destruction and repair and then assessed their individual contributions in this process. We show that ligature-induced periodontal remodelling occurred in response to both inflammation and changes to mechanical loading. Bmp2 and Bmp7 showed dynamic expression changes following injury, with early upregulation in the periodontium including the root apex, where Gli1$^+$ PDL stem cells (PDLSCs) reside. Gli1$^+$ PDLSCs are multipotent and contribute to tissue regeneration. Deletion of Bmp2 or Bmp7 in Gli1$^+$ PDLSCs significantly delayed periodontium regeneration. Bmp2, but not Bmp7, was required for efficient expansion of Gli1$^+$ PDLSCs, as its deletion reduces lineage traced cells. Loss of Bmp2 was furthermore associated with loss of cementum-lining lineage-traced cells, while Bmp7-dependent lineage-traced cells were predominantly located within the periodontal space. Together, Bmp2 and Bmp7 are both induced early after injury and required for efficient repair of the periodontium, however with distinct contributions during the early phase of periodontal repair. These distinct requirements for PDLSC expansion and differentiation highlight functional differences between Bmp2 and Bmp7 for periodontal regeneration.

Highlights

1. The ligature-induced periodontal injury model triggers both inflammation- and mechanically-driven bone loss and remodelling.
2. Bmp2 and Bmp7 are rapidly induced following ligature placement preceding periodontal repair with restricted and discrete expression observed along the root apex.
3. Deletion of *Bmp2* or *Bmp7* in Gli1$^+$ PDLSCs delays periodontal tissue regeneration and alveolar bone formation revealing discrete roles of these two Bmps, with Bmp2 contributing to the expansion of Gli1$^+$ PDLSC expansion in response to injury.

INTRODUCTION

Periodontitis is among the most common inflammatory conditions affecting humans,[1] leading to progressive destruction of the supporting structures of the teeth, including the alveolar bone.[2] This destruction often culminates in tooth loss if left untreated.[3] The primary goal of periodontal therapy is not only to halt disease progression but also to regenerate the lost tissues, especially the alveolar bone.[4,5] To this end, emerging regenerative strategies, including the application of growth factors, cell-based therapies, and gene therapies, have been explored.[6–8] Treatment with recombinant bone

morphogenetic proteins (Bmps), specifically Bmp2 and Bmp7, have shown promising effects on periodontal regeneration and have been used clinically.[9,10] However, their biological functions extend beyond simply promoting bone formation.[11] Bmp signaling regulates a wide spectrum of cellular behaviors, including osteoblast differentiation, osteoclast activity, and mesenchymal stem cell fate decisions, thereby likely playing a complex role in maintaining skeletal tissue homeostasis.[12,13] In the context of the periodontium, this complexity is particularly relevant but poorly understood.

The periodontium consists of root cementum, periodontal ligament (PDL), and alveolar bone. The PDL harbors a pool of periodontal ligament stem cells (PDLSCs), which are essential for the development, maintenance, and regeneration of periodontal tissues.[14] A key aspect of periodontal regeneration is the osteogenic differentiation of PDLSCs into osteoblasts, tightly regulated by transcription factors and growth factors, including Bmps.[15,16] To date, most studies have investigated the effect of osteoinductive Bmps regulate PDLSCs on the hard tissue differentiation *in vitro*.[17,18] Little is known on how Bmps regulate PDLSCs proliferation and differentiation *in vivo*.

The ligature-induced periodontitis model has been widely used as a preclinical animal model to understand human periodontitis and tissue repair.[19] For instance, a recent investigation used Bmp7-engineered bone marrow stromal cell (Bmp7-eBMSC) transplantation to demonstrate improved regeneration of alveolar bone and the PDL.[20] However, the rapid bone loss observed in this model is uncharacteristic for human periodontal disease. It remains unclear if the observed bone loss is solely the result of inflammation or if other processes such as altered mechanical loading are also involved. There is also limited information on the potential involvement of endogenous Bmps in progression of periodontal injury, inflammation, and tissue repair. To study the latter aspect, the ligature model has been adapted to study both PDL/bone loss (catabolic phase) and regeneration (anabolic phase) following ligature removal.[21–23] This provides an ideal framework to elucidate the temporal and spatial expression patterns of different Bmps in the periodontium during disease progression and repair, as well as to clarify if they have distinct roles in coordinating interactions among osteoblasts, osteoclasts, and PDLSCs.

The periodontium remodels in response to changes in compressive loading such as changes in occlusion or mastication.[24] Yes-associated protein (YAP) signaling is a key mediator of this response.[25–28] YAP is a mechanosensitive transcriptional regulator that responds to mechanical cues such as extracellular matrix rigidity, strain, shear stress, and adhesive area.[29] Its activity is tightly controlled by multiple pathways, including Hippo signaling mediated by cell polarity, Wnt-YAP/TAZ interactions, G protein-coupled receptor signaling, metabolic regulation, and crosstalk with growth factor and inflammatory signaling pathways, in a highly context-dependent manner.[30] YAP directs mesenchymal stem cell (MSC) differentiation via its activity in shuttling between the nucleus (active-YAP) and cytoplasm (p-YAP).[31] Nuclear translocation of YAP facilitates MSC migration and drives subsequent osteogenic differentiation.[32]

Previous lineage-tracing studies have identified multiple PDLSC populations within the PDL, including Gli1$^+$, Axin2$^+$, LepR$^+$, and Prx1$^+$ cells, that contribute to periodontal repair and regeneration.[33–36] Long-term lineage-tracing experiments demonstrated that approximately 85% of osteocytes in alveolar bone are derived from Gli1$^+$ PDLSCs, and injury-activated Gli1$^+$ cells play a pivotal role in alveolar bone repair.[37] Given that Gli1$^+$ PDLSCs serve as a major cellular source for osteogenic differentiation, they represent an ideal population to study how Bmps regulates PDLSC activity during periodontal hard tissue regeneration.

In this study, we describe the temporal expression and localization of Bmp2 and Bmp7 in the periodontium using the ligature injury model. We provide evidence that altered mechanical loading significantly contributes to bone remodelling, in particular at the root apex. Targeting Bmp2 and Bmp7 in Gli1$^+$ PDLSCs, we show that these Bmps are independently required for efficient alveolar bone repair. Bmp2, but not Bmp7, is critical for amplification of Gli1$^+$ PDLSC and subsequent bone/cementum remodeling, while Bmp7's role appears to be more directed to periodontal remodelling. Both Bmps are required in PDLSCs to guide efficient alveolar bone and PDL regeneration.

RESULTS

Ligature placement induces rapid and broad catabolic activity along the entire tooth

We first determined sites and kinetics of bone/PDL remodeling following ligature placement/removal. Buccolingual sections were assessed using Hematoxylin/Eosin (H/E), Tartrate-resistant acidic phosphatase (TRAP), and Picrosirius Red (PSR) staining at days 7, 14, 28, and 35 (Fig. 1a). The non-ligature control side showed a smooth alveolar bone surface with few TRAP-positive cells present at the root apex and furcation at all time points (Fig. 1b, non-lig). PSR staining revealed well-organized and densely packed PDL collagen fibers oriented between the alveolar bone and cementum, consistent with normal PDL architecture (Fig. 1c, non-lig). In contrast, the ligature side showed irregular alveolar bone surfaces with abundant TRAP-positive signal on days 7 and 14 (Fig. 1b). PSR staining revealed a pronounced disorganization of PDL collagen fibers along the entire length of the root (Fig. 1c). Following ligature removal at day 21, TRAP positivity was minimal at days 28 and 35, and the bone surfaces regained their smoothness (Fig. 1b). Correspondingly, PSR staining revealed partial to substantial reorganization of PDL collagen fibers at days 28 and 35 (Fig. 1c). These findings were consistent with µ-CT analysis, where alveolar bone had irregular surfaces on the ligature side from day 7 to day 14 with a wider PDL space when compared to the non-ligature side (Fig. 1b).

PDL remodeling occurs in response to inflammation and altered mechanical loading

To assess extracellular matrix remodeling within the PDL more directly, we stained for collagen type I alpha 1 (Col1a1). At both day 7 and day 14 post-ligation, Col1a1 was prominently detected in PDL cells lining both mineralized interfaces, including the alveolar bone surface and the root apical cellular cementum (Fig. 2a, e), indicating active matrix-remodeling at these sites. To assess the degree of inflammation, we probed for the presence of inflammatory cells using the common leukocyte antigen (CD45). Clustered $CD45^+$ cells were restricted to the gingiva margin and the alveolar bone crest matching the inflammatory infiltrate evident on H/E-stained sections (Fig. 2b). CD45-staining was largely absent from deeper PDL areas or the root apex sections (Fig. 2f), though CD45-positivity was noted in some cells, most likely osteoclasts. Consistent with this spatially restricted inflammatory response, IL-17a-staining was similarly restricted to the gingival margin and alveolar bone crest regions at days 7 and 14, with minimal signal detected in the deeper PDL or toward the root apex (Fig. 2c, g). This restricted inflammatory microenvironment suggests that mechanisms other than inflammation are responsible for the apical resorption of mineralized tissue observed in Fig. 1b. Given the strong remodelling of collagen fibers, we thus assessed changes to mechanical stimulation using Ser127 phosphorylated Yes-associated protein (p-Yap), a well-established readout of mechanical signaling.[38] P-Yap expression was observed in the PDL cells along the entire tooth on day 7 and 14 (Fig. 2d, h), suggesting that altered mechanical loading significantly ($p < 0.001$) contributes to PDL and alveolar bone remodelling. Staining for active Yap showed similar expression (Fig. S1), further supporting the involvement of mechanical signaling in this process.

Alveolar bone resorption extends beyond ligated regions, supporting a contribution of mechanical force in the ligature model.

To further corroborate changes in loading environment as a source of alveolar bone loss, we examined the adjacent first molar, which did not receive ligature placement. Micro–computed tomography (micro-CT) revealed progressive structural changes at the first molar palatal root with clear evidence of alveolar bone loss by Day 7 compared to baseline (Day 0) (Fig. 3a). Higher-magnification views reveal a widening of the PDL space on the ligature side (Fig. 3b), indicative of alveolar bone resorption in the absence of overt inflammation at this site. Multinucleated Cathepsin K $(Ctsk)^+$ osteoclasts were observed along the alveolar bone surface on the ligature side, with minimal staining on the non-ligature control (Fig. 3c), and H/E staining revealed irregular bone surfaces (Fig. 3f). In contrast, $CD45^+$ inflammatory cells remained largely confined to the gingival tissues and were not detected in the PDL or apical region (Fig. 3d), indicating that inflammation cannot account for the observed bone resorption. Notably, phosphorylated Yap (p-Yap) expression was increased in PDL cells on the ligature side (Fig. 3e), suggesting altered mechanical signaling. Quantification confirmed reduced bone volume (Fig. 3h–i) and increased $Ctsk^+$ osteoclasts and $p\text{-}Yap^+$ cells, while $CD45^+$ cell numbers remained low (Fig. 3j–l). Together, these findings indicate that alveolar bone resorption extending to adjacent non-ligated teeth occurs largely independent of local inflammation, supporting a role for mechanically driven remodeling in the ligature model.

Limited expression of Bmps in healthy adult mouse periodontium.

To assess expression of osteogenic Bmp ligands in periodontal tissue under homeostatic conditions, we analyzed a published single-cell RNA sequencing (scRNA-seq) dataset of adult mouse molar periodontal ligament cells [GEO Access number: GSE197828][39]. Unsupervised clustering revealed distinct cell populations within the periodontium (Fig. 4a). *Bmp2, Bmp4, Bmp5, Bmp6*, and *Bmp7* were expressed at low levels in several cell populations (Fig. 4b). *Bmp2* and *Bmp7* were relatively higher expressed when compared to other Bmp ligands. Visualization of individual Bmp expression indicated discrete and only partly overlapping expression patterns (Fig. 4d–h). Focusing on *Bmp2* and *Bmp7*, we observed partly overlapping expression in $CD200^+$ bone progenitor cells, but largely distinct expression in mesenchymal progenitor cell subpopulations (Fig. 4c). Together, these findings identify Bmp2 and Bmp7 as the predominant osteogenic Bmps in adult mouse periodontium under homeostatic conditions. These findings were validated in an independent scRNA-seq dataset (Fig. S2) [GEO Access number: GSE160358][40].

Bmp2 and Bmp7 are both induced during the catabolic phase following ligature placement.

Bmp2 and Bmp7 showed little and weak expression in PDL under homeostasis (non-ligature) but were strongly induced during the catabolic phase within the PDL and along irregular bone surfaces (Fig. 5a). Interestingly, Bmp2 and Bmp7 displayed a distinct distribution within the PDL. Bmp2 was frequently observed around cells lining the bone surface, whereas Bmp7 appeared more broadly distributed within the PDL. During the anabolic phase of the model, expression of Bmp2 and Bmp7 was comparatively less. Comparing the root apex and the alveolar bone crest area revealed that the overall expression kinetic was comparable, albeit a delay in expression was noted in the crest area. Other Bmps (Bmp5 and Bmp6) were also detected following ligature placement (Fig. S3). Canonical Bmp signaling, assessed via pSmad1/5/9, was widespread throughout the PDL on day 7 (Fig. S4), indicating broadly active Bmp signaling. We next mapped $Sp7^+$ osteoblasts and $Ctsk^+$ osteoclasts during the catabolic (days 7–14) and anabolic (days 28–35) phases of the ligature model. Sp7 and Ctsk expression were detected at the alveolar bone crest as well as the root apex (Fig. 6a). $Sp7^+$ cells were markedly increased in cells lining the bone surface and root apex at days 7 and 14 when compared to the non-ligature control side. $Sp7^+$ cells remained elevated at day 28 but slowly reduced in numbers by day 35. $Ctsk^+$ cells also significantly increased on days 7 and 14. Expression was predominantly localized to large multi-nucleated cells along the bone surface, likely osteoclasts. In contrast, Ctsk immunoreactivity was virtually absent at days 28 and 35, in line with the lack of TRAP staining at those timepoints. The observed expression of Bmp2 and Bmp7 in relation to bone-forming or -resorbing cells suggests that early following ligature placement Bmp2 might act on both bone-forming or -resorbing cells, while Bmp7 was more often observed within the PDL space. Quantification confirmed that Bmp ligands, $Sp7^+$ osteoblasts, and $Ctsk^+$ osteoclasts were all significantly elevated during the catabolic phase (days 7–14) compared to both non-ligature controls and the anabolic phase (days 28–35) (Fig. 5b-e; Fig. 6b-e).

Bmp deletion in $Gli1^+$ PDLSCs compromises periodontal remodelling

To investigate if deletion of *Bmp2* or *Bmp7* in Gli1⁺ PDLSCs affects periodontal remodelling and regeneration, we induced *Bmp2* or *Bmp7* deletion in adult Gli1-CreERt2 mice and challenged the mice subsequently with the ligature-induced periodontal injury model (Fig. 7a). To assess the contribution of Bmp2 and Bmp7 to periodontal remodelling, we first analyzed the 1st molar, both at the non-ligature and ligature side. Histological analysis at D35 on H/E-stained sections on first molar revealed signs of remodelling at the ligature side of all mice, including non-treated control wildtype mice. In contrast to controls and tamoxifen-injected wildtype mice, both *Bmp2*- and *Bmp7*-mutants showed irregular alveolar bone surfaces at the ligature side compared to non-ligature controls, indicating compromised bone remodelling (Fig. 7c–f). The presence of Gli1⁺ PDLSC-derived cells was assessed using lineage tracing of GFP expression in Cre-recombined cells. At the apex of the root, GFP^+ cells were abundant; many appeared to be associated with vasculature irrespective of ligature placement. However, within the periodontium, the ligature side teeth exhibited an increased number of GFP⁺ cells compared to non-ligature side teeth (Fig. 7g, i), which was confirmed by quantitative analysis (Fig. 7h, j). Comparable results were observed at the second molar, where ligature-side teeth showed increased GFP⁺ cells within the periodontium (Fig. 7k, l). *Bmp2*cKO mutants displayed consistently fewer GFP⁺ cells in the periodontal ligament and gingival space compared to *Bmp7*cKO mutants (Fig. 7m, n). These findings indicate that Bmp2, but not Bmp7, is required for efficient expansion of Gli1⁺ PDLSCs during periodontal regeneration.

Deletion of Bmp2 or Bmp7 in Gli1$^+$ PDLSCs Impairs Alveolar Bone Regeneration

To investigate whether Bmp2 or Bmp7 deletion in Gli1⁺ PDLSCs affects alveolar bone regeneration following periodontal injury, we analyzed tissue morphology and bone architecture at day 35 after ligature-induced injury. H/E staining of the second molar revealed structural differences between control and mutant mice. At the ligature side, both *Bmp2*cKO and *Bmp7*cKO mice exhibited irregular alveolar bone surfaces and widened PDL spaces compared to controls, indicating impaired tissue recovery (Fig. 8a–c). Regions of newly formed bone and areas lacking proper regeneration were evident in overlaid micro-CT images comparing day 0 and day 35 (Fig. 8d–f). Micro-CT analysis at day 35 confirmed the increased PDL space around the injured teeth in both *Bmp2*cKO and *Bmp7*cKO mutant mice when compared to controls (Fig. 8g). Quantification revealed that in addition to a wider PDL (Fig. 8h), the original bone volume could not be regained (Fig. 8i). Despite these defects in alveolar bone recovery, some cementum formation at the root apex which occurs in response to ligature placement[23] was still observed in both *Bmp2*cKO (Fig. 8j-l) and *Bmp7*cKO (Fig.S5) mutants. Thus, while alveolar bone regeneration is impaired, the capacity for cementogenesis is at least partially preserved in both mutants.

GFP lineage tracing reveals limited osteolineage contribution of Gli1⁺ PDLSCs following ligature-induced injury

To evaluate the osteogenic contribution of Gli1⁺ PDLSCs during periodontal regeneration, we compared lineage tracing with immunofluorescence analysis of osteogenic markers at the root apical region.

Regions of interest (ROIs) were defined based on DAPI staining of tooth and surrounding periodontal tissues (Fig. 9a). Immunofluorescence staining revealed distinct expression patterns of osteogenic markers in both *Bmp2*cKO and *Bmp7*cKO mice. Runx2$^+$ cells were detected along the alveolar bone surface but were largely absent from the cellular cementum region (Fig. 9b). Sp7$^+$ cells were abundant and distributed along both alveolar bone and cellular cementum surfaces, with some Sp7$^+$ cells embedded within the cementum matrix. Interestingly, comparison of *Bmp2*- with *Bmp7*-mutants revealed a difference in location of Sp7$^+$ cells, which showed clustering along the cementum surface in *Bmp7*-mutants while they were more dispersed into the PDL space in *Bmp2*-mutants. Pdgfr-β$^+$ cells were observed in close proximity to these osteogenic regions, particularly along the alveolar bone surface, displaying a localization pattern similar to Sp7$^+$ cells. Micro-CT analysis further demonstrated dynamic changes in alveolar bone morphology following ligature placement and removal. At day 14, irregular bone surfaces indicative of active resorption was evident (Fig. 9c, white arrows), whereas by day 35, these surfaces appeared smoother, consistent with ongoing bone remodeling after ligature removal. Lineage tracing of GFP$^+$ cells revealed limited contribution of Gli1$^+$-derived cells to osteocyte populations within the alveolar bone. In the periosteal region, GFP$^+$ osteocytes were more readily detected in *Bmp7*cKO mice, whereas they were sparse in *Bmp2*cKO mice (Fig. 9d), suggesting a reduced contribution of Gli1$^+$ progeny to bone remodeling in the absence of Bmp2. Similarly, fewer GFP$^+$ cells associated with the cementum in *Bmp2*cKO mice compared to *Bmp7*cKO mice (Fig. 9e). Together, this analysis reveals discrete differences between *Bmp2*cKO and *Bmp7*cKO mice including the root apex, periodontal space, as well as periosteum, suggesting non-redundant roles of Bmp2 and Bmp7 in periodontal remodelling.

DISCUSSION

The ligature-induced periodontitis mouse model is one of the most widely used approaches in preclinical periodontal research.[41] However, unlike the chronic, microbiome-driven dysbiosis and gradual tissue destruction observed in patients, the ligature model represents an acute periodontal injury response during the first 2 weeks after ligature placement.[21] Our study supports this distinction, showing that ligature placement induces acute inflammation–associated periodontal injury, with extensive bone resorption occurring throughout the alveolar bone area. Therefore, while it provides valuable insights into bone resorption and bone regeneration, its limitations in replicating the disease's multifactorial nature must be acknowledged.

Inflammatory cells were predominantly found around the ligature site, along with the peak of CD45 expression at day 7, suggests that inflammation is highly localized in this model; this is further supported by elevated IL-17a expression at the ligature site. Apical bone loss occurring without significant inflammatory cell infiltration points to non-inflammatory mechanisms, such as mechanical stress[42] or altered loading conditions,[43] being responsible for the remodeling in the apical region. The detection of p-Yap and active Yap in the root apical area supports the notion and that changes to mechanical loading may influence mesenchymal stem cell responses contributing to bone

remodeling.[44,45] However, definite distinction between mechanosensation and inflammation is difficult, as Yap is also involved in inflammatory responses, including monocyte adhesion to inflamed endothelium and macrophage activation.[46,47] As p-Yap/Yap expression was not confined to inflammatory cells or mediators that show a restriction of the inflammation to the upper half of the root and Yap/p-Yap expression was also observed at a more distant root at the first molar, this suggests a contribution of altered mechanosensation to the observed bone loss. Furthermore, an *in vitro* study demonstrated mechano-responsive regulation of Col1a1 in human PDL fibroblasts subjected to cyclic stretching or force loading,[48] our Col1a1 expression patterns are consistent with a potential contribution of altered mechanical conditions to extracellular matrix remodeling in the periodontal ligament. Based on the above, the ligature model should be viewed as ligature-induced periodontal injury model rather than a ligature-induced periodontitis model.

We described changes to expression and localization of Bmp2 and Bmp7 over the 35-day period of the model. Both Bmp2 and Bmp7 were most strongly expressed during the catabolic phase of the model and thus their role in tissue repair might be particularly important in the early stages. Furthermore, Bmp2 was associated with both osteoblasts (Sp7) and osteoclasts (Ctsk) supporting multifaceted roles for Bmp2[13,49] also *in vivo*. Notably, within the PDL, both Bmp2 and Bmp7 appeared to localize around individual cells, with little evidence of their diffusion into surrounding areas. This restricted pattern suggests that Bmp signaling in the PDL primarily acts through localized autocrine or short-range paracrine mechanisms, as might be expected in the light of tightly regulated tissue remodeling and repair. This cell-restricted localization further implies that regenerative responses in the PDL depend on the discrete local production of these ligands. Clinically, recombinant human Bmp2 is used in bone grafts and implants with the expectation of promoting bone regeneration.[50] Demonstrating the timing and localization of Bmp2 expression during the early but not later phases of bone formation suggests that application of recombinant Bmp2 should best follow this ‘natural regenerative window’ to minimize side effects of this therapy.[51] In addition, the observed restricted endogenous expression within the PDL raises concerns that broad application of exogenous recombinant human Bmp2 will not be able to fully recapitulate endogenous Bmp signaling, as previously shown.[52]

$Gli1^+$ PDL cells have been identified as mesenchymal stem cells with potential to differentiate into osteoblasts during alveolar bone regeneration,[53] while $Gli1^+$ periosteal skeletal stem/progenitor cells contribute to periosteal skeletal repair.[54] Gli1-creERT2 was used to investigate how Bmp2 and Bmp7 affect alveolar bone and periodontal regeneration. Deletion of either *Bmp* resulted in delayed periodontal regeneration. This finding was somewhat surprising, as gene deletion was induced 10 − 7 days prior to ligature placement and Cre-mediated recombination was restricted to Gli1-expressing cells. Given the scarcity of $Gli1^+$ cells at the root apex,[37] we were initially not confident that this strategy would target sufficient progenitor cells to evoke a phenotypic change. Interestingly, the survival/expansion of $Gli1^+$ progenitors was comprised specifically in *Bmp2* mutants, indicating a non-redundant role for Bmp2 for expansion of $Gli1^+$ progenitor cells. We did not investigate if other PDLSCs that were not targeted by our

approach, such as Sox9^{+} and Axin2^{+} populations, were also affected. Bmp2 might be particularly important for progenitor cells, as conditional inducible deletion of Bmp2 in more mature cell types such as osteoblasts or endothelial cells did not impair bone formation following injury or mechanical loading in adult mice.[55] As Sp7^{+} cells were observed in close vicinity to Pdgfr-β expressing cells (Fig. 9b), osteoblast precursors might also be derived from perivascular mesenchymal progenitor cells, which have been shown to have bone-forming potential[56] and at least in part contribute to Gli1^{+}-derived progenitors (Fig. 9b). Our preferred interpretation is that progenitor cells rather than osteoblasts are the source and target of Bmp2 at the root apex and that Gli1^{+}-cells coordinate subsequent periodontal repair. Together, our data suggests that Bmp2 more likely orchestrates progenitor recruitment and expansion in line with its role in the periosteum[57,58] rather than driving terminal osteogenic differentiation within the PDL.

Why bone repair was delayed in both Bmp2 and Bmp7 mutants, while the number of Gli1^{+} cells was only reduced in the absence of Bmp2 will need to be addressed in future studies. There is likely an underappreciated interdependence of different PDLSCs populations and signals that coordinate periodontal repair that involves different Bmps. Immunofluorescence localization of Bmp2 and Bmp7 showed clear differences, with Bmp7 more broadly expressed within rather than lining the PDL space (Fig. S6). In that context, it is interesting to note that induced deletion of *Bmp2* or *Bmp7* resulted in a slightly different location of lineage-traced cells within the periodontium, mirroring differences in expression. Future studies will require spatial transcriptomics of periodontal tissues during homeostasis and repair in wild-type but also Bmp-mutant mice to untangle the discrete transcriptional and functional programs of the various progenitor and differentiating cells *in vivo*.

MATERIALS AND METHODS

Animal and Experimental Design

All animal experimental procedures were reviewed and approved by the University of Alberta Animal Care and Use Committee (AUP1648), in accordance with federal guidelines.

Wild-type Mice for Bmp Detection

We employed a ligature-induced periodontal injury model in 8-week-old C57BL/6J wild-type mice as described.[23] The ligature was removed on day 21, and the study continued until day 35. Mice were randomly divided into four experimental groups (n = 6 per group; total = 24 mice, 1:1 male-to-female ratio). The contralateral, non-ligated side of the maxilla served as an internal control. Each animal had one tooth ligated and served as biological replicate.

Conditional Knockout Mice for Functional Analysis

Gli1-CreERt2 (JAX:007913) mice were crossed to mT/mG gene reporter mice (JAX:007676) as well as *Bmp2* fl/fl;mT/mG$^{tg/tg}$ (*Bmp2*cKO) or *Bmp7* fl/fl;mT/mG$^{tg/tg}$ (*Bmp7*cKO).[59] Tamoxifen (20 mg/ml in corn oil) was administered intraperitoneally (100 µl daily for 4 consecutive days) to induce Cre recombinase activity specifically in Gli1^{+}PDLSCs. *Bmp2*cKO (n = 5) and *Bmp7*cKO (n = 5) and control (n = 5) mice were subject to the ligature-induced periodontal injury model.

Tamoxifen administration

Tamoxifen (Sigma-Aldrich, T5648-1G) was dissolved in corn oil at a concentration of 20 mg/mL by shaking overnight and administered via intraperitoneal injection at a dose of 100 µl per mouse (~ 2 mg per mouse, corresponding to ~ 100 mg/kg for a 25 g mouse) once daily for 4 consecutive days. Mice were 8 weeks old at the start of tamoxifen administration. To allow sufficient Cre-mediated recombination and clearance of tamoxifen, the ligature-induced periodontal injury was performed 7 days after the final injection. Throughout the course of tamoxifen injections and any post injection wait period, mice should be closely monitored for any adverse reactions to the treatment.

Tissue Collection

Mice were euthanized and perfused with 4% paraformaldehyde (PFA) (Thermo Scientific 41678-0010). Heads were fixed in 4% PFA for 24 hours, decalcified in 0.5 M EDTA (Fisher Chemical™ S311-500) pH 7.4 for 4 weeks, then embedded in paraffin. Serial sagittal sections (7 µm) were prepared for histological and immunostaining analyses.

Live µCT Scanning

Mice were anesthetized with isoflurane (1–3% in oxygen) to minimize movement and subjected to micro-CT (µCT) imaging using a Milabs UHT-µCT scanner (Milabs, Utrecht, The Netherlands). All scans were acquired under the following settings: 1440 projections, 75 ms exposure, 0.24 mA current, 50 kV voltage, with an angle of 0.25 degrees. The focused irradiation dose per scan under these settings was 1.67 Gy. Scans were reconstructed using Milabs software at a 25-micron voxel size. 3D reconstructions were saved in NIFTI file format.

3D Slicer application

Micro-CT datasets of mouse skull were processed using 3D Slicer software (version 5.6.2). The following modules were employed: Volume Rendering, Crop Volume, Segmentation, Segment Editor, and Segment Statistics. To ensure accurate comparisons across samples and timepoints, scan alignment was performed prior to any further operation. All scans were rotated and adjusted to a standard anatomical orientation based on cranial landmarks. Comparable 2D views were used to captured slightly changes (Fig. 2a, b; Fig. 9c; Fig. S7a-d). The Crop Volume module was then used to isolate the alveolar bone ROI, reducing file size and focusing the analysis on the relevant anatomical area. ROI boundaries were set using fixed anatomical landmarks to ensure reproducibility. To reduce variability in longitudinal analyses of the same sample, the ROI was first defined at baseline (day 0). This same ROI box was then consistently applied across subsequent time points for that sample (Fig. S7a-c), allowing for reliable

tracking of alveolar bone changes over time without the need for repeated ROI selection. Within the defined ROI, segmentation of alveolar bone was performed using the Segmentation module (Fig. S7e). The periodontal ligament space was measured on a 2D view at the second molar (Fig. S7f), where both lingual and buccal roots are visible, using the lingual root due to its relatively straight morphology.

Deparaffinize and rehydrate slides

Put slides in oven for 10 min at 60°C, or until wax melts. Wash slides in the following solutions: 10 min xylene; 10 min xylene; 10 min 100% ethanol; 10 min 100% ethanol; 5 min 95% ethanol; 5 min 70% ethanol; 5 min water bath.

Hematoxylin/ Eosin (H/E) staining

H/E (Hematoxylin/ Eosin) staining was employed to evaluate overall tissue morphology and changes in the alveolar bone. After deparaffinization and rehydration of the tissue sections, the samples were immersed in hematoxylin solution (Fisher Chemical™ 200 – 100) for approximately 5 minutes, allowing for adequate staining of the cell nuclei. Following hematoxylin staining, the sections were rinsed in running tap water for 3 minutes, then incubated in bluing solution for 3 minutes to enhance nuclear contrast. Subsequently, the sections were placed in eosin solution for 2 minutes to stain the cytoplasm and extracellular matrix. The excess eosin was removed by washing the sections in distilled water. Sections were dehydrated through a series of graded ethanol solutions (70%, 95%, and 100%), followed by clearing in xylene. Finally, the slides were mounted with Permount™ mounting medium (Fisher Chemical™ SP15-100) for microscopic examination. H/E-stained slides were scanned and digitally converted into virtual slides using a ZEISS Axioscan 7 Slide Scanner. Virtual slides were viewed and analyzed using the ZEN blue viewer software.

Tartrate Resistant Acid Phosphatase (TRAP) staining

After deparaffinization and rehydration, the sections were incubated in pre-warmed TRAP staining solution (TRAP Basic Incubation Medium 25ul; Fast Red Violet LB Salt (Sigma-Aldrich F3381-1G) 15mg; Naphthol AS-MX Phosphate Substrate mix 125 ul) at 37°C for 30 minutes, closely monitored until a bright violet stain indicating osteoclast activity was observed. The sections were then rinsed in distilled water and counterstained with 0.02% Fast Green (Sigma-Aldrich F7252-5G) for 2 minutes. Following several additional washes in distilled water, the sections were thoroughly air-dried and mounted with Permount™ mounting medium (Fisher Chemical™ SP15-100). TRAP-stained slides were scanned and digitally converted into virtual slides using a ZEISS Axioscan 7 Slide Scanner. Virtual slides were viewed and analyzed using the ZEN blue viewer software.

Picrosirius Red (PSR) staining

Paraffin sections were deparaffinized and rehydrated, followed by staining with 1% Alcian Blue for 30 min. Sections were rinsed in 1% acetic acid for 5 min, washed in distilled water for 5 min, and then incubated in Picrosirius Red solution for 1 h. During Picrosirius Red staining, slides were gently agitated

every 15 min to ensure uniform staining. Sections were rinsed twice in acidified water, dehydrated, cleared, and mounted with Permount™ mounting medium.

Immunofluorescence (IF) staining

For IF analyses, the following primary antibodies were used: anti-Bmp2 (1:200; ab94744; Abcam, Cambridge, MA, USA), anti-Bmp7 (1:200; ab84684; Abcam, Cambridge, MA, USA), anti-Sp7 (1:1000; ab209484; Abcam, Cambridge, MA, USA), anti-p-YAP (1:100; 4911S; Cell Signaling Technology, Danvers, MA, USA), anti-Col1A1 (1:200; E8F4L; Cell Signaling Technology, Danvers, MA, USA), anti-p-SMAD1/5/9 (1:100; 13820S; Cell Signaling Technology, Danvers, MA, USA), anti-CD45 (1:400; sc53665; Santa Cruz Biotechnology, Dallas, TX, USA), anti-IL17a (1:200; 26163-1-AP; Proteintech, Rosemont, IL, USA), anti-Runx2 (1:200; Sc-390351; Santa Cruz Biotechnology, Dallas, TX, USA), and anti-CTSK (1:400; sc48353; Santa Cruz Biotechnology), anti-Bmp5 (1:200; 13253-1-AP; Proteintech, Rosemont, IL, USA), anti-Bmp6 (1:200; 13253-1-AP; Proteintech, Rosemont, IL, USA), anti-GFP (1:1000; ab290; Abcam, Cambridge, MA, USA), active YAP1 (1:300; ab205270; Abcam, Cambridge, MA, USA). The following secondary antibodies were used: donkey anti-rabbit IgG H&L (1:1,000; A31573; Alexa Fluor 647-conjugated; Thermo Fisher Scientific, Waltham, MA, USA), goat anti-mouse IgG H&L (1:1000; A31573; Alexa Fluor 647-conjugated; Thermo Fisher Scientific, Waltham, MA, USA), and goat anti-rat IgG H&L (1:1000; A21247; Alexa Fluor 647-conjugated; Thermo Fisher Scientific). Stained slides were mounted with a medium containing Dabco (Sigma 290734) Mowiol 4–88 (Sigma 81381) (DM).

After deparaffinization and rehydration, sections were incubated in microwaved Tris-EDTA buffer (pH 9.0) for antigen retrieval. Sections were rinsed in phosphate-buffered saline (3x5 min) before being covered with blocking serum for 45 min to block non-specific binding. Following blocking incubation, primary antibody was added to the sections and incubated overnight at 4°C. After another round of rinses/washes, the secondary antibody was incubated for 2 h at room temperature. Sections were counterstained with DAPI (4,6-diamidino-2-phenylindole) for nuclear staining. Primary antibody was replaced with 1% bovine serum albumin phosphate-balanced saline for the negative staining controls. The images were acquired on a ZEISS Axioscan 7 Slide Scanner.

Quantification of IF staining

Quantification of immunofluorescence staining was performed by counting positively stained cells within defined regions of interest (ROIs) in the root apical periodontal ligament (PDL) and the top of the alveolar bone crest (ABC). For each ROI, three sections from different experimental mice were analyzed. Only sections that contain comparable anatomical landmarks—including the tooth root, adjacent PDL, and surrounding alveolar bone—were selected for analysis to ensure consistency across samples. The root apical PDL ROI was defined as the PDL region adjacent to the root apex, while the ABC ROI was defined at the coronal region of the alveolar bone crest. ROIs of identical size and shape were applied to all sections at the same relative position. Besides PDL ROI and ABC ROI, we had specific ROI definition. For Col1a1, the ROI encompassed the root apical region, including the root tip and the immediately adjacent PDL cell layers, to quantify Col1a1 expression in PDL cells neighboring the apical root

cementum. For CD45, the ROI included the mid-root PDL region below the gingiva, while excluding the coronal PDL adjacent to the ligature and the inflamed gingival tissue, in order to avoid areas of acute injury-associated inflammatory infiltrate. For p-Yap, the ROI was defined in the mid-root PDL and used to assess p-Yap expression in the PDL cells. Cathepsin K (Ctsk)–positive multinucleated cells and CD45 positive cells were counted directly. The ratios of positively stained cells were calculated for p-Yap, active Yap, Bmp2, Bmp7, and Sp7. The ratios of Fluoresce Area to ROI area were calculated for Col1a1. The intensity of Fluoresce was calculated for IL17a.

Statistical analysis

All data are presented as mean ± standard deviation (SD) and analyzed using GraphPad Prism10.0. Statistical significance was assessed using two-tailed Student's t-test for two-group comparisons. Immunofluorescence staining was quantified using ImageJ software. At least three independent experimental replicates were conducted, and representative images were selected. $P < 0.05$ was considered statistically significant.

Single-cell RNA sequencing (scRNA-seq) analysis

scRNA-seq analysis was performed using publicly available scRNA-seq datasets (Mouse PDL mRNA profiles during adult homeostasis). Data can be found at GEO; Access number: GSE197828, GSE160358. Raw sequencing data were processed using the Seurat package. Low-quality cells were excluded based on gene number and mitochondrial gene content. Data were normalized, scaled, and subjected to principal component analysis, followed by unsupervised clustering and UMAP dimensionality reduction. Cell populations were annotated based on established marker gene expression, and differential gene expression analysis was performed between identified cell clusters.

DATA AVAILABILITY

Original data has been deposited on the BioImage Archive (www.ebi.ac.uk) under S-BIAD2846. Additional data generated for this study are available from the corresponding author upon request.

Declarations

Running title

Bmp2 and Bmp7 in periodontal injury and repair

CONFLICT OF INTERESTS

There are no competing interests due to relationships or undisclosed funding sources.

AUTHOR CONTRIBUTIONS

Yu Fu contributed to conception and design of the study, acquired, analyzed and interpreted data, drafted and critically revised the manuscript. Daniela M Roth contributed to design of the study, acquired data, and critically revised the manuscript. Maria Alexiou contributed design of the study, acquired data, and critically revised the manuscript. Daniel Graf contributed to conception and design of the study, acquired, analyzed and interpreted data, acquired funding, drafted and critically revised the manuscript. All authors gave final approval and agree to be accountable for all aspects of work ensuring integrity and accuracy.
The authors would like to acknowledge Farah Eaton for her extensive experimental assistance and data collection.

ACKNOWLEDGEMENTS

This study received support from the Alberta Institute at Wenzhou Medical University (AIWMU) (YF), Alberta Dental Association & College Chair in Oral Health Research (DG) and NSERC Discovery grant (RGPIN-2022-03272) to DG.

References

1. GBD 2016 Disease and Injury Incidence and Prevalence Collaborators. Global, regional, and national incidence, prevalence, and years lived with disability for 328 diseases and injuries for 195 countries, 1990–2016: a systematic analysis for the Global Burden of Disease Study 2016. Lancet Lond. Engl. 390, 1211–1259 (2017).
2. Li, Y., Ling, J. & Jiang, Q. Inflammasomes in Alveolar Bone Loss. Front. Immunol. 12, 691013 (2021).
3. Kinane, D. F., Stathopoulou, P. G. & Papapanou, P. N. Periodontal diseases. Nat. Rev. Dis. Primer 3, 17038 (2017).
4. Liu, J. et al. Periodontal Bone-Ligament-Cementum Regeneration via Scaffolds and Stem Cells. Cells 8, 537 (2019).
5. Tomokiyo, A., Wada, N. & Maeda, H. Periodontal Ligament Stem Cells: Regenerative Potency in Periodontium. Stem Cells Dev. 28, 974–985 (2019).
6. Liang, Y., Luan, X. & Liu, X. Recent advances in periodontal regeneration: A biomaterial perspective. Bioact. Mater. 5, 297–308 (2020).
7. Ding, T., Kang, W., Li, J., Yu, L. & Ge, S. An in situ tissue engineering scaffold with growth factors combining angiogenesis and osteoimmunomodulatory functions for advanced periodontal bone regeneration. J. Nanobiotechnology 19, 247 (2021).
8. Angjelova, A. et al. Insights and Advancements in Periodontal Tissue Engineering and Bone Regeneration. Med. Kaunas Lith. 60, 773 (2024).
9. Rao, S. M., Ugale, G. M. & Warad, S. B. Bone morphogenetic proteins: periodontal regeneration. North Am. J. Med. Sci. 5, 161–168 (2013).

10. Kaur, S., Grover, V., Kaur, H. & Malhotra, R. Evaluation of bone morphogenic proteins in periodontal practice. Indian J. Dent. 7, 28–37 (2016).
11. Blázquez-Medela, A. M., Jumabay, M. & Boström, K. I. Beyond the bone: Bone morphogenetic protein signaling in adipose tissue. Obes. Rev. Off. J. Int. Assoc. Study Obes. 20, 648–658 (2019).
12. Zhang, L. et al. Transcriptomic landscape regulated by the 14 types of bone morphogenetic proteins (BMPs) in lineage commitment and differentiation of mesenchymal stem cells (MSCs). Genes Dis. 6, 258–275 (2019).
13. Bordukalo-Nikšić, T., Kufner, V. & Vukičević, S. The Role Of BMPs in the Regulation of Osteoclasts Resorption and Bone Remodeling: From Experimental Models to Clinical Applications. Front. Immunol. 13, 869422 (2022).
14. Wen, W. et al. Osteogenic mesenchymal stem cells/progenitors in the periodontium. Oral Dis. 30, 914–920 (2024).
15. Yan, S., Zhang, M., Yang, G., Sun, Y. & Ai, D. CTGF Promotes the Osteoblast Differentiation of Human Periodontal Ligament Stem Cells by Positively Regulating BMP2/Smad Signal Transduction. BioMed Res. Int. 2022, 2938015 (2022).
16. Harris, S. E., Rediske, M., Neitzke, R. & Rakian, A. Periodontal Biology: Stem Cells, Bmp2 Gene, Transcriptional Enhancers, and Use of Sclerostin Antibody and Pth for Treatment of Periodontal Disease and Bone Loss. Cell Stem Cells Regen. Med. 3, (2017).
17. Hyun, S.-Y., Lee, J.-H., Kang, K.-J. & Jang, Y.-J. Effect of FGF-2, TGF-β-1, and BMPs on Teno/Ligamentogenesis and Osteo/Cementogenesis of Human Periodontal Ligament Stem Cells. Mol. Cells 40, 550–557 (2017).
18. Wang, L. et al. NELL1 augments osteogenesis and inhibits inflammation of human periodontal ligament stem cells induced by BMP9. J. Periodontol. 93, 977–987 (2022).
19. Lin, P. et al. Application of Ligature-Induced Periodontitis in Mice to Explore the Molecular Mechanism of Periodontal Disease. Int. J. Mol. Sci. 22, 8900 (2021).
20. Jung, Y.-H. et al. Regenerative Potential of Bone Morphogenetic Protein 7-Engineered Mesenchymal Stem Cells in Ligature-Induced Periodontitis. Tissue Eng. Part A 29, 200–210 (2023).
21. de Molon, R. S., Park, C. H., Jin, Q., Sugai, J. & Cirelli, J. A. Characterization of ligature-induced experimental periodontitis. Microsc. Res. Tech. 81, 1412–1421 (2018).
22. Viniegra, A. et al. Resolving Macrophages Counter Osteolysis by Anabolic Actions on Bone Cells. J. Dent. Res. 97, 1160–1169 (2018).
23. Fu, Y. et al. A reliable micro-CT-based method reveals dynamic changes to alveolar bone and tooth root following ligature-induced periodontal injury in the mouse. Bone 201, 117619 (2025).
24. Wen, X., Pei, F., Jin, Y. & Zhao, Z. Exploring the mechanical and biological interplay in the periodontal ligament. Int. J. Oral Sci. 17, 23 (2025).
25. Zhou, Y., Zhang, G. & He, H. Mechanical forces orchestrate the epigenetic landscape of oral mesenchymal stem/progenitor cell fate in dental and periodontal tissues. Front. Cell Dev. Biol. 14,

1743397 (2026).
26. Dong, X. et al. Tooth Movement Modulation and Root Protection via Piezo1-Mediated Production of Superoxide Dismutase 3. J. Periodontal Res. https://doi.org/10.1111/jre.70056 (2026) doi:10.1111/jre.70056.
27. Meng, X. et al. The cytoskeleton dynamics-dependent LINC complex in periodontal ligament stem cells transmits mechanical stress to the nuclear envelope and promotes YAP nuclear translocation. Stem Cell Res. Ther. 15, 284 (2024).
28. Zhang, X. et al. YAP/WNT5A/FZD4 axis regulates osteogenic differentiation of human periodontal ligament cells under cyclic stretch. J. Periodontal Res. 58, 907–918 (2023).
29. Elosegui-Artola, A. et al. Force Triggers YAP Nuclear Entry by Regulating Transport across Nuclear Pores. Cell 171, 1397–1410.e14 (2017).
30. Yamashiro, Y. et al. Matrix mechanotransduction mediated by thrombospondin-1/integrin/YAP in the vascular remodeling. Proc. Natl. Acad. Sci. 117, 9896–9905 (2020).
31. Ghagre, A., Delarue, A., Srivastava, L. K., Koushki, N. & Ehrlicher, A. Nuclear curvature determines Yes-associated protein localization and differentiation of mesenchymal stem cells. Biophys. J. 123, 1222–1239 (2024).
32. Guo, Y. et al. HtrA3 paves the way for MSC migration and promotes osteogenesis. Bioact. Mater. 38, 399–410 (2024).
33. Zhang, D. et al. Lepr-Expressing PDLSCs Contribute to Periodontal Homeostasis and Respond to Mechanical Force by Piezo1. Adv. Sci. Weinh. Baden-Wurtt. Ger. 10, e2303291 (2023).
34. Zhao, J., Faure, L., Adameyko, I. & Sharpe, P. T. Stem cell contributions to cementoblast differentiation in healthy periodontal ligament and periodontitis. Stem Cells Dayt. Ohio 39, 92–102 (2021).
35. Deng, Y. et al. Gli1 + Periodontal Mesenchymal Stem Cells in Periodontitis. J. Dent. Res. 103, 279–288 (2024).
36. Gong, X. et al. Tracing PRX1 + cells during molar formation and periodontal ligament reconstruction. Int. J. Oral Sci. 14, 5 (2022).
37. Men, Y. et al. Gli1 + Periodontium Stem Cells Are Regulated by Osteocytes and Occlusal Force. Dev. Cell 54, 639–654.e6 (2020).
38. Feng, F. et al. Mechano-growth factor regulates periodontal ligament stem cell proliferation and differentiation through Fyn-RhoA-YAP signaling. Biochem. Biophys. Res. Commun. 733, 150450 (2024).
39. Iwayama, T. et al. Plap-1 lineage tracing and single-cell transcriptomics reveal cellular dynamics in the periodontal ligament. Development 149, dev201203 (2022).
40. Zhao, J., Faure, L., Adameyko, I. & Sharpe, P. T. Stem cell contributions to cementoblast differentiation in healthy periodontal ligament and periodontitis. Stem Cells 39, 92–102 (2021).

41. Wu, Y.-H. et al. Dynamic microstructural changes in alveolar bone in ligature-induced experimental periodontitis. Odontology 108, 339–349 (2020).
42. Tsutsumi, T. et al. Micro-computed tomography for evaluating alveolar bone resorption induced by hyperocclusion. J. Prosthodont. Res. 62, 298–302 (2018).
43. Wang, L., You, X., Zhang, L., Zhang, C. & Zou, W. Mechanical regulation of bone remodeling. Bone Res. 10, 16 (2022).
44. Kim, E. et al. YAP mechanotransduction under cyclic mechanical stretch loading for mesenchymal stem cell osteogenesis is regulated by ROCK. Front. Bioeng. Biotechnol. 11, 1306002 (2023).
45. Deng, J. et al. Mechanosensor YAP mediates bone remodeling via NF-κB p65 induced osteoclastogenesis during orthodontic tooth movement. Prog. Orthod. 26, 2 (2025).
46. Meli, V. S. et al. YAP-mediated mechanotransduction tunes the macrophage inflammatory response. Sci. Adv. 6, eabb8471 (2020).
47. Wang, K.-C. et al. Flow-dependent YAP/TAZ activities regulate endothelial phenotypes and atherosclerosis. Proc. Natl. Acad. Sci. 113, 11525–11530 (2016).
48. Kook, S.-H. et al. Mechanical force induces type I collagen expression in human periodontal ligament fibroblasts through activation of ERK/JNK and AP-1. J. Cell. Biochem. 106, 1060–1067 (2009).
49. Li, F. et al. Efficacy of Recombinant Human BMP2 and PDGF-BB in Orofacial Bone Regeneration: A Systematic Review and Meta-analysis. Sci. Rep. 9, 8073 (2019).
50. Priddy, L. B. et al. Amniotic membrane attenuates heterotopic ossification following high-dose bone morphogenetic protein-2 treatment of segmental bone defects. J. Orthop. Res. Off. Publ. Orthop. Res. Soc. 41, 130–140 (2023).
51. Atasoy-Zeybek, A. et al. Efficient autocrine and paracrine signaling explain the osteogenic superiority of transgenic BMP-2 over rhBMP-2. Mol. Ther. - Methods Clin. Dev. 29, 350–363 (2023).
52. Shalehin, N. et al. Gli1+-PDL Cells Contribute to Alveolar Bone Homeostasis and Regeneration. J. Dent. Res. 101, 1537–1543 (2022).
53. Jeffery, E. C., Mann, T. L. A., Pool, J. A., Zhao, Z. & Morrison, S. J. Bone marrow and periosteal skeletal stem/progenitor cells make distinct contributions to bone maintenance and repair. Cell Stem Cell 29, 1547–1561.e6 (2022).
54. McBride-Gagyi, S. H., McKenzie, J. A., Buettmann, E. G., Gardner, M. J. & Silva, M. J. Bmp2 conditional knockout in osteoblasts and endothelial cells does not impair bone formation after injury or mechanical loading in adult mice. Bone 81, 533–543 (2015).
55. Wang, Z. et al. Pdgfrβ marks distinct mesenchymal and pericyte populations within the periosteum with overlapping cellular features. Stem Cells Dayt. Ohio 43, sxaf020 (2025).
56. Julien, A. et al. Skeletal Stem/Progenitor Cells in Periosteum and Skeletal Muscle Share a Common Molecular Response to Bone Injury. J. Bone Miner. Res. 37, 1545–1561 (2020).

57. Papageorgiou, P. et al. Expanded skeletal stem and progenitor cells promote and participate in induced bone regeneration at subcritical BMP-2 dose. Biomaterials 217, 119278 (2019).
58. Graf, D. & Economides, A. N. Dissection of bone morphogenetic protein signaling using genome-engineering tools. Bone Morphog. Proteins Local Syst. Ther. 115–139 (2008).

Figures

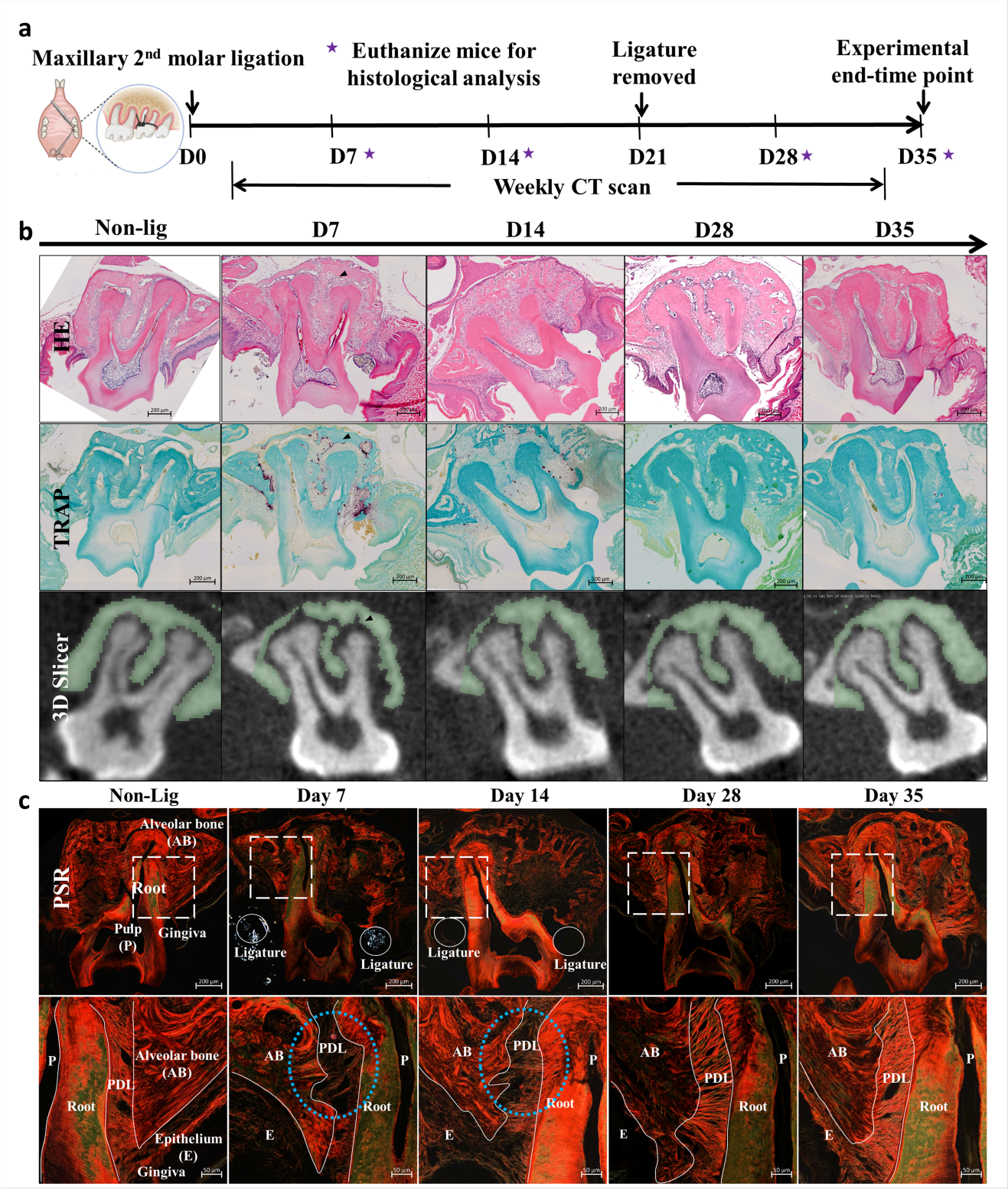


Figure 1

Histological analysis of alveolar bone remodeling following ligature-induced periodontal injury in wild type mice. (a) Experimental design and timeline. Ligature silks were placed on day 0 and removed on day 21. Frontal sections of fixed, decalcified skulls were collected at days 7, 14, 28, and 35 for histological (H/E), TRAP and Picrosirius Red (PSR) staining. Mice were CT scanned weekly. **(b)** Representative H/E and TRAP-stained buccolingual sections of non-ligature and ligature sides. Corresponding 3D Slicer CT scan reconstructions show widened PDL space and irregular bone surfaces at early time points. Black arrow heads point out bone resorption at root apical area. **(c)**Picrosirius Red (PSR) staining of the periodontal ligament (PDL) in non-ligature control and ligature-side teeth at days 7, 14, 28, and 35. Ligature-side teeth show disorganized collagen fibers (blue circle) along the entire root at days 7 and 14, followed by partial to substantial reorganization at days 28 and 35.

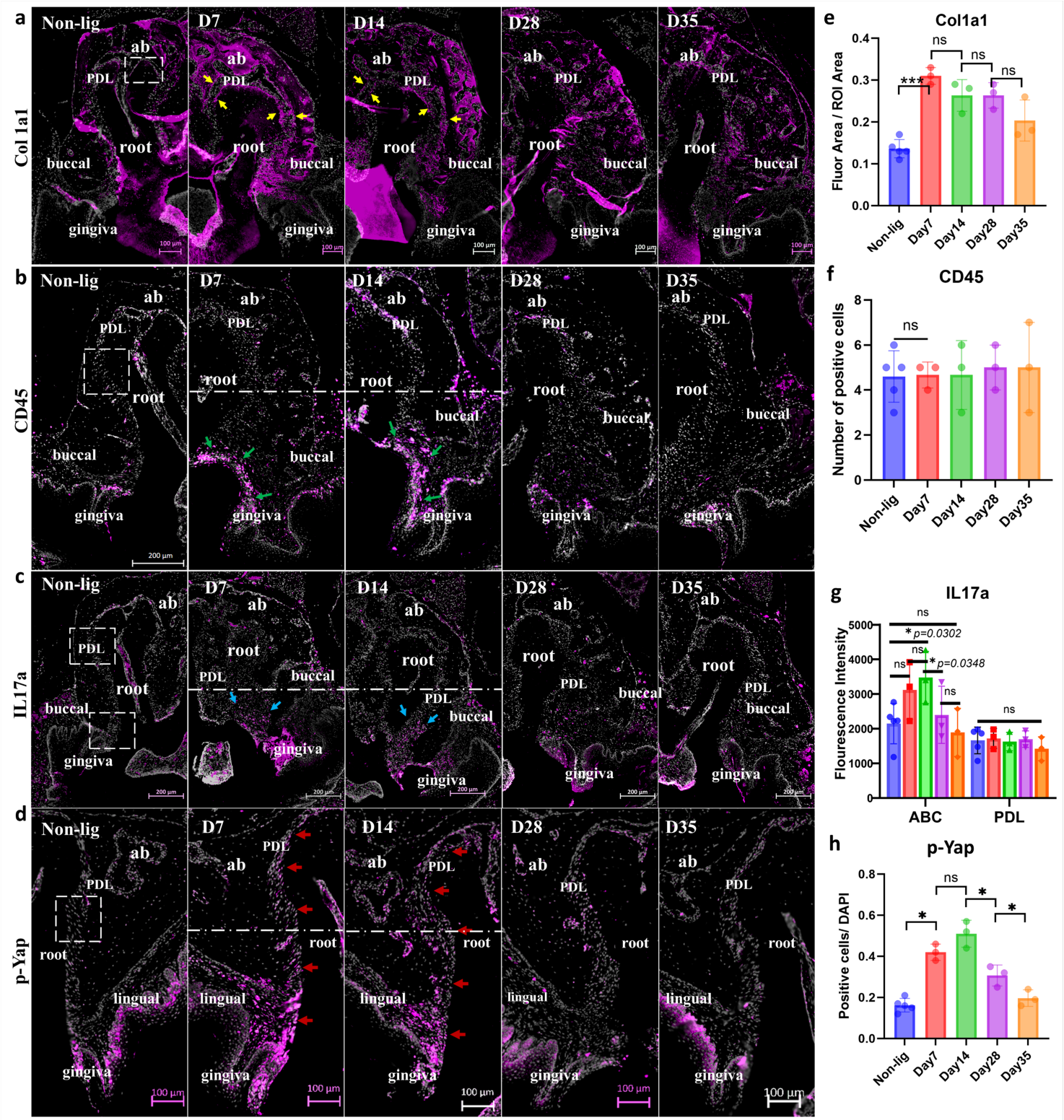


Figure 2

Spatial patterns of matrix remodeling, inflammation, and mechanotransduction in the periodontal ligament. (a) Immunofluorescence staining for Collagen type I alpha 1 (Col1a1) in buccolingual sections of non-ligature controls and ligature-side teeth at days 7, 14, 28, and 35. Scale bar: 100 μm.**(b)** CD45 staining at days 7, 14, 28, and 35. Clustered inflammatory cells at the gingival margin and alveolar bone crest on ligature teeth at days 7 and 14 (green arrows). Scale bar: 200 μm. The white dotted line

delineates the separation between the alveolar bone crest (ABC) region and the root apical region. **(c**) IL-17astaining at days 7, 14, 28, and 35. Blue arrows indicate the boundary of IL-17a staining. Scale bar: 200 μm. **(d)** Phosphorylated Yap (p-Yap) is broadly distributed throughout the PDL along the tooth length on ligature teeth at days 7 and 14 (red arrows). Scale bar: 100 μm. All panels show representative half-tooth sections including crown, gingiva, PDL, root, root apex, and alveolar bone. Non-ligature contralateral teeth serve as controls. **(e-h)** Quantification of Col1a1, CD45, IL-17a and p-Yap–positive staining within the indicated white ROIs. Statistical significance is denoted as *P < 0.05, ***P < 0.001; ns, not significant.

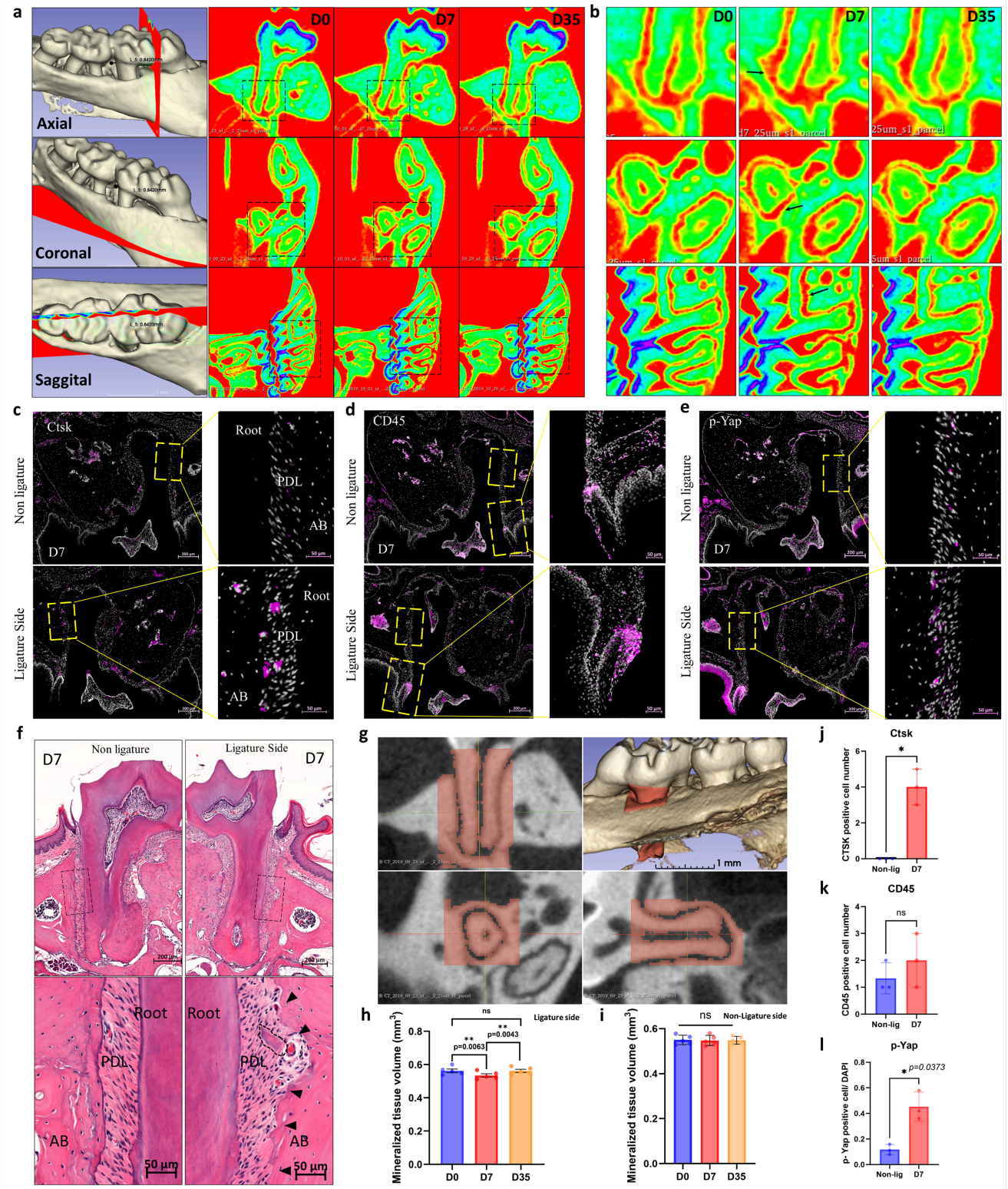


Figure 3

Alveolar bone resorption extends beyond ligated regions, supporting a contribution of mechanical force in the ligature model. (a) Representative micro–computed tomography (micro-CT) images showing axial, coronal, and sagittal views of the palatal root of the first molar at Days 0, 7 and 35. following ligature placement on the second molar. **(b)** Higher-magnification images of the palatal root region demonstrating widening of the periodontal ligament (PDL) space (black arrows) on the ligature

side. **(c)** Cathepsin K (Ctsk) immunostaining showing multinucleated osteoclasts along the alveolar bone surface on the ligature side, with minimal staining on the non-ligature side. **(d)** CD45 immunostaining demonstrating that inflammatory cell infiltration is largely confined to the gingival tissue. **(e)** phosphorylated-Yap (p-Yap) immunostaining showing increased expression in the PDL on the ligature side compared to the non-ligature control. **(f)** H/E staining of the palatal root region revealing irregular alveolar bone surfaces on the ligature side, consistent with active bone resorption (black arrowheads). **(g)**Representative image indicating the region of interest (ROI) used for alveolar bone analysis in micro-CT. **(h-i)** Quantification of alveolar bone volume within the defined ROI. **(j-k)** Quantification of $Ctsk^+$ osteoclasts, $CD45^+$ inflammatory cells, and $p\text{-}Yap^+$ cells in the analyzed region. Statistical significance is denoted as *P < 0.05, ***P < 0.001; ns, not significant.

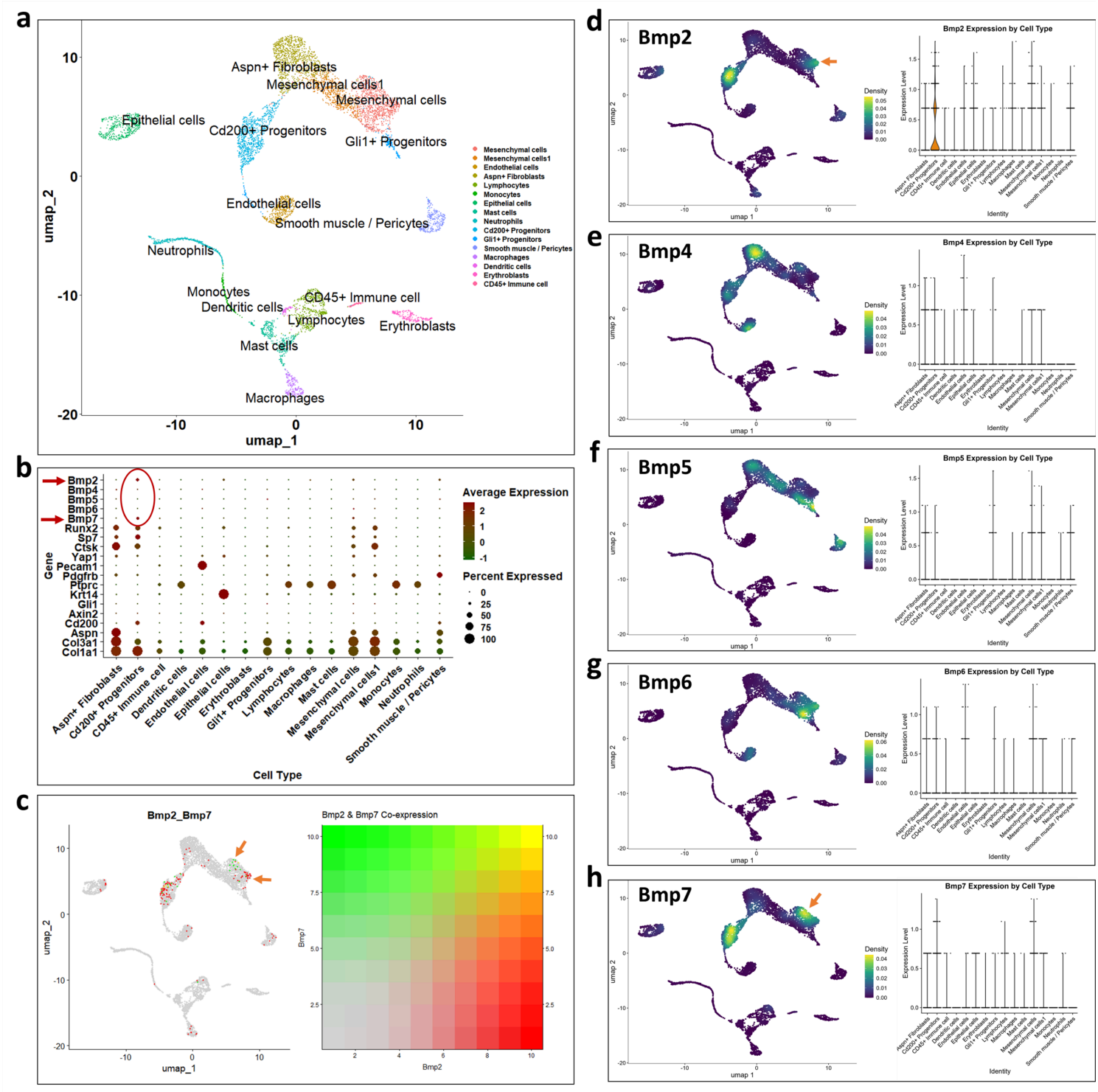


Figure 4

scRNA-seq identifies *Bmp2* as the predominant osteogenic Bmp in the adult mouse periodontium. (a) UMAP plot showing the distribution of identified cell types in the adult mouse molar periodontal ligament. **(b)**Dotplot illustrates the expression of osteogenic Bmp genes (*Bmp2, Bmp4, Bmp5, Bmp6 and Bmp7*) across different cell types. *Bmp2* and *Bmp7*exhibit relatively higher expression levels (red arrows). **(c)**Co-expression feature plots of *Bmp2* and *Bmp7*. Although these genes display similar overall distribution patterns across clusters, the co-expression plot reveals enrichment of trends within two

subclusters (orange arrows). **(d-h)** Expression profiles of *Bmp2, Bmp4, Bmp5, Bmp6* and *Bmp7*across the identified cell clusters, showing the distribution and relative expression levels of these genes among cell types. Data can be found at GEO; Access number: GSE197828.

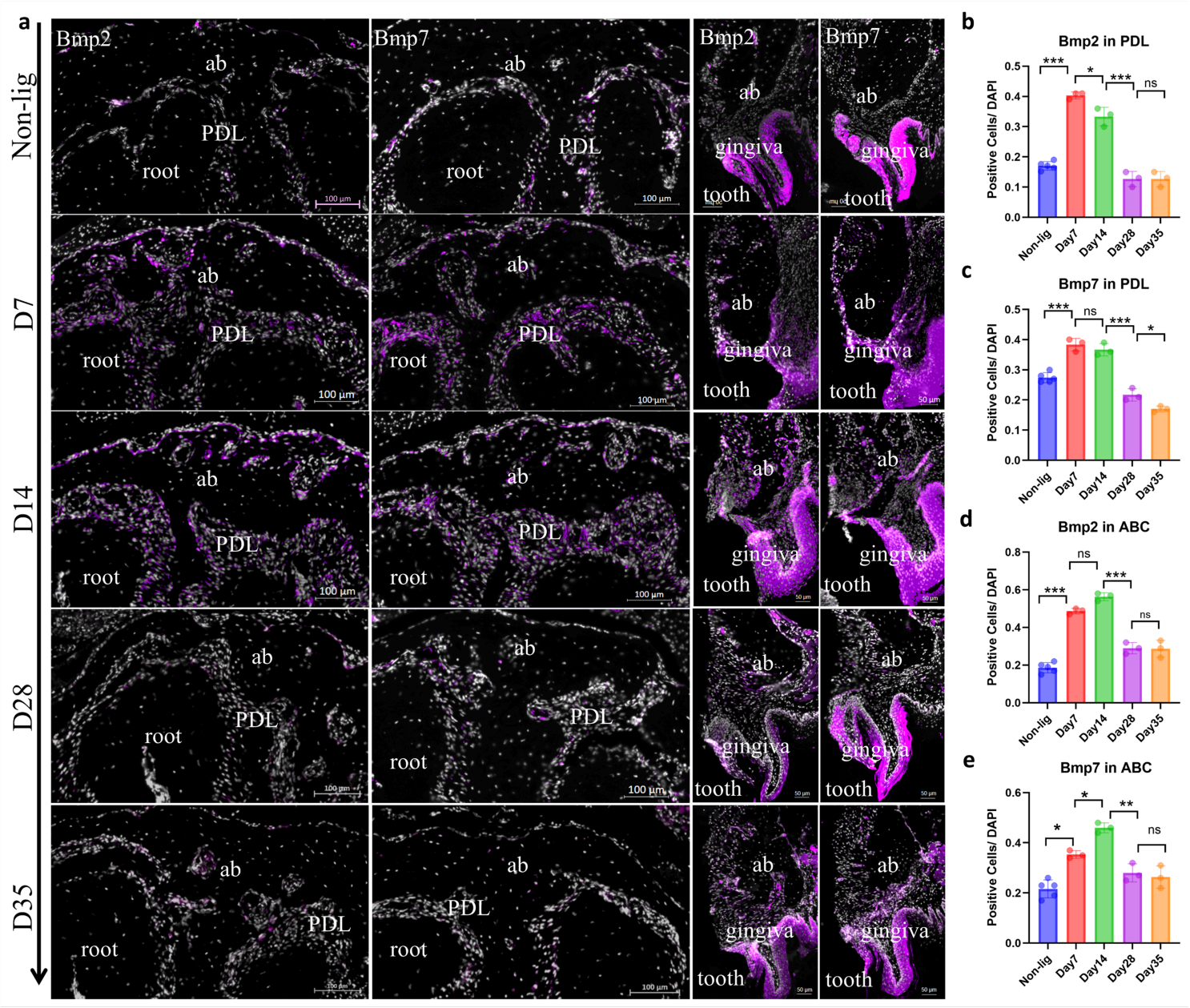


Figure 5

Temporal dynamics of Bmp2 & 7 expression in periodontal remodeling. (a) Representative immunofluorescence staining of Bmp2 and Bmp7 (purple) in periodontal tissues across the same time course (days 7, 14, 28, 35). Both were elevated at days 7–14, with Bmp2 localized along bone surfaces and Bmp7 broadly distributed in the periodontal ligament (PDL); expression was minimal by days 28-35. **(b-e)** Quantification of Bmp2⁺ and Bmp7⁺ cells corresponding to panel (a). Data are presented as the percentage of Bmp-positive cells relative to total DAPI⁺ nuclei (Positive cells/DAPI) within the analyzed

regions of interest. Data were obtained from at least three independent biological replicates per experiment. Statistical significance is denoted as *P < 0.05, **P < 0.01, ***P < 0.001; ns, not significant.

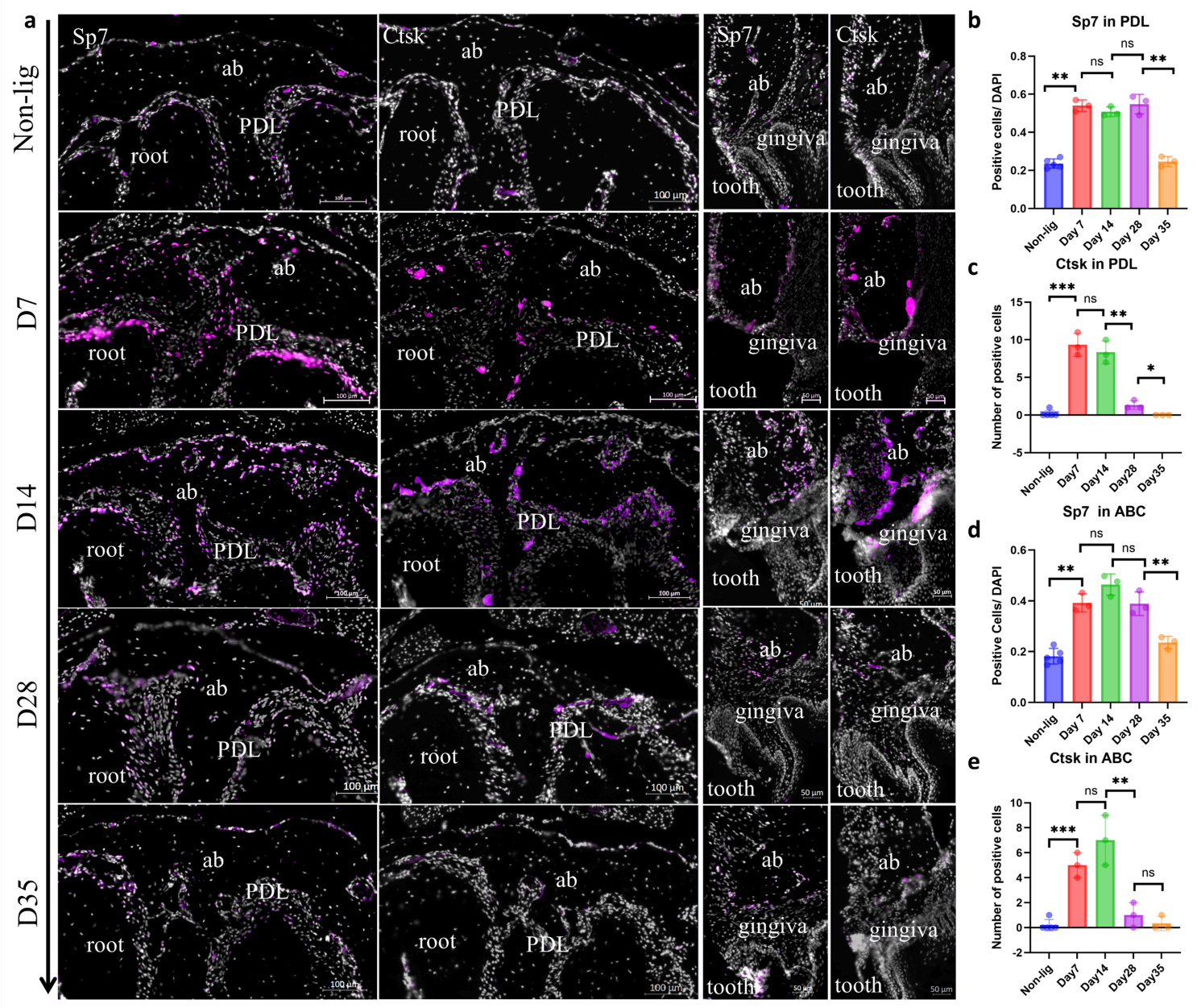


Figure 6

Temporal dynamics of osteoblast/osteoclast activity in periodontal remodeling.
(a) Immunofluorescence staining of Sp7 (osteoblast marker, purple) and Cathepsin K (Ctsk, osteoclast marker, purple) in the root apical and alveolar bone crest regions at different time points (days 7, 14, 28, 35). Nuclei were counterstained with DAPI (white). **(b-e)** Quantification of Sp7⁺ and Ctsk⁺ cells corresponding to panel (a). Sp7 expression was quantified as the percentage of Sp7⁺ cells relative to total DAPI⁺ nuclei (positive cells/DAPI) within the defined regions of interest (Root apical PDL and Alveolar bone crest). Ctsk expression was quantified by counting the number of Ctsk⁺ multinucleated

osteoclasts per section. Data were obtained from at least three independent biological replicates per experiment. Statistical significance is denoted as *P < 0.05, **P < 0.01, ***P < 0.001; ns, not significant.

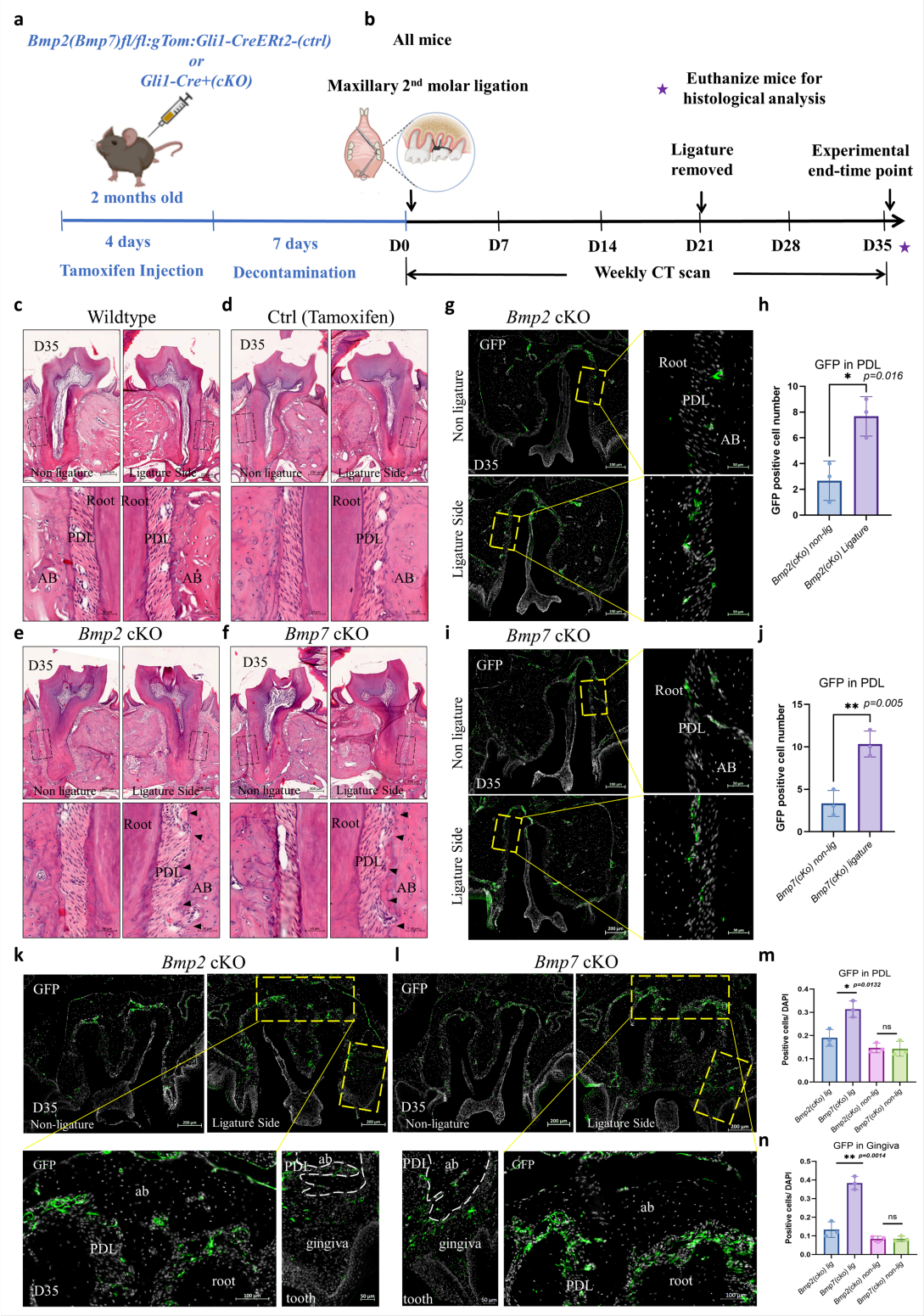


Figure 7

***Bmp2* deletion in Gli1⁺ PDLSCs impairs progenitor expansion. (a-b)** Schematic of experimental design using *Bmp2*$^{fl/fl}$: Gli1-CreERt2 and *Bmp7*$^{fl/fl}$: Gli1-CreERt2 mice with ligature-induced periodontal injury. **(a)**

Two-month-old *Bmp2*$^{fl/fl}$: gTom; Gli1-CreERt2 or *Bmp7*$^{fl/fl}$: gTom; Gli1-CreERt2 mice and Cre-negative littermate controls received tamoxifen inductions for 4 consecutive days, followed by a 7-day decontamination period prior to ligature placement on the maxillary second molar. **(b)** Ligatures were placed at day 0 (D0), removed at day 21 (D21). Mice were analyzed by weekly micro-CT and collected on the D35 for histology. **(c-f)** Representative H/E-stained buccolingual sections of non-ligature and ligature sides on first molar. Black arrow heads point out irregular alveolar bone surfaces on the ligature side tooth. **(g)** GFP labeling of Gli1$^+$ PDLSCs in the first molar from *Bmp2*cKO mutants. **(h)** Quantification of GFP$^+$ PDLSCs in the PDL (n=3). **(i)** GFP labeling of Gli1$^+$ PDLSCs in the first molar from *Bmp7*cKO mutants. **(j)** Quantification of GFP$^+$ PDLSCs in the PDL (n=3). **(k)** GFP labeling of Gli1$^+$ PDLSCs in the second molar from *Bmp2*cKO mutants. **(l)** GFP labeling of Gli1$^+$ PDLSCs in the second molar from *Bmp7*cKO mutants. **(m)** Quantification of GFP$^+$ PDLSCs in the PDL (n=3). **(n)** Quantification of GFP$^+$ PDLSCs in the Gingiva (n=3). Data were obtained from at least three independent biological replicates per experiment. Statistical significance is denoted as *P < 0.05, **P < 0.01, ***P < 0.001; ns, not significant.

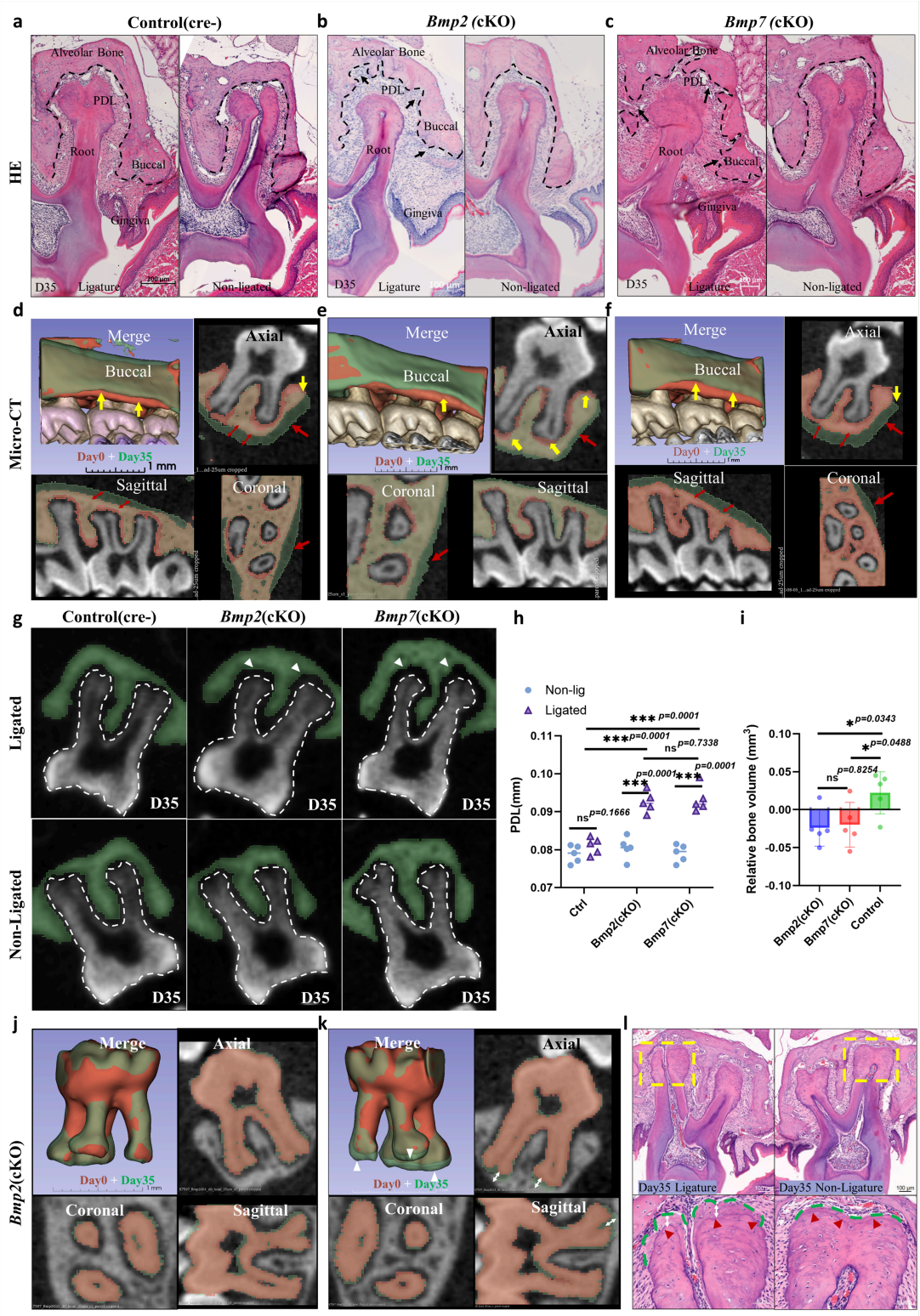


Figure 8

Inducible deletion of *Bmp2*or *Bmp7* in Gli1⁺ PDLSCs impairs alveolar bone regeneration. (a-c) H/E staining of non-ligature and ligature sides on second molar. The black arrows highlight irregular bone surfaces and wilder PDL spaces in both *Bmp2*cKO and *Bmp7*cKO mice compared to controls. **(d-f)** Overlaid micro-CT images of alveolar bone at day 0 (red) and day 35 (green) illustrating incomplete restoration of the alveolar bone (yellow arrows) and new established bone during bone remodeling (red

arrows). **(g)** Representative micro-CT slices showing enlarged PDL space (white arrowheads) in *Bmp2*cKO and *Bmp7*cKO mice compared to controls at day 35. **(h)** Quantitative measurements of PDL width. **(i)** Quantitative measurements of alveolar bone volume.**(j-k)** Overlaid micro-CT images of second molars (day 0 red; day 35 green) showing root apex cementum deposition (white arrowheads) in *Bmp2*cKO mutant mice. **(l)** Cementum formation is evident in H/E; Red arrowheads indicate a dark stain line separating newly formed cementum from original cementum. Statistical significance is indicated (*P < 0.05, **P < 0.01, ***P < 0.001; ns, not significant).

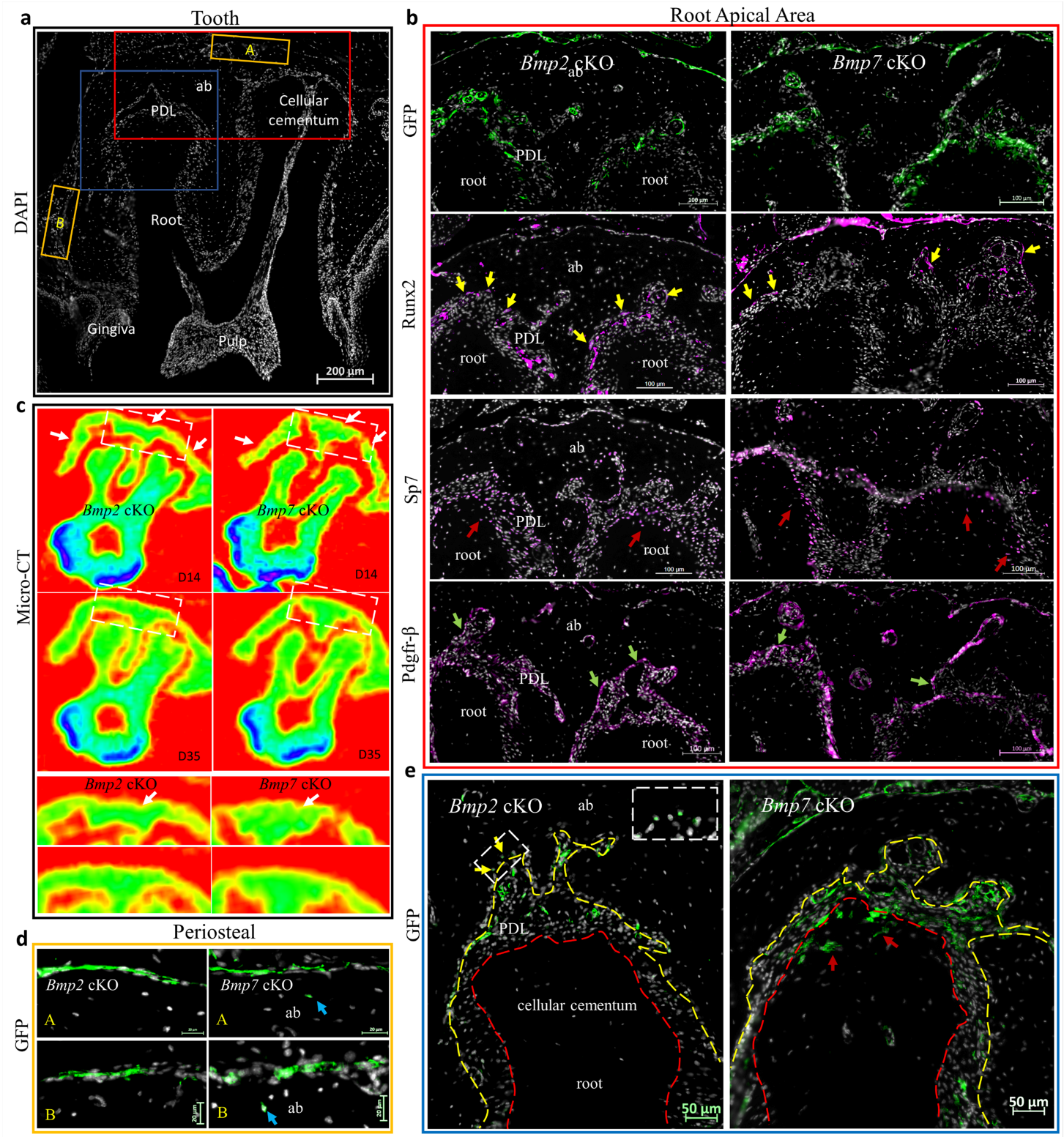


Figure 9

GFP lineage tracing of Gli1⁺ cells reveal impaired osteolineage contribution following ligature-induced injury. (a) Representative DAPI staining of tooth and surrounding periodontal tissues. Colored boxes indicate regions of interest (ROIs). **(b)** Immunofluorescence staining of the root apical region (red ROI) showing GFP, Runx2, Sp7, and Pdgfr-β expression in *Bmp2*cKO and *Bmp7*cKO mice. Runx2⁺ cells (yellow arrows) are detected along the alveolar bone surface but are absent on the cellular cementum side in both models. Sp7⁺ cells line both alveolar bone and cellular cementum surfaces, with Sp7⁺ cells within cementum indicated by red arrows. Pdgfr-β⁺ cells are indicated by green arrows. **(c)** Micro-CT analysis at day 14 (D14) and day 35 (D35) after ligature placement. White arrows indicate ligature-induced bone resorption at D14 and subsequent bone remodeling following ligature removal at D35. **(d)** GFP⁺ cells in the periosteal region. Osteocytes (blue arrows) are evident in *Bmp7*cKO but limited in *Bmp2*cKO mice. **(e)** GFP staining in the root apical region. Yellow arrows indicate osteocytes in *Bmp2*cKO, while red arrows indicate cementoblasts in *Bmp7*cKO.

Supplementary Files

This is a list of supplementary files associated with this preprint. Click to download.

- SupplementaryMaterialYFv3IJOS.pdf